THE JOURNAL OF PHYSICAL CHEMISTRY C

Article

Electronic Structure of Vertically Aligned Mn-Doped CoFeO Nanowires and Their Application as Humidity Sensors and Photodetectors

Chang Hyun Kim, Yoon Myung, Yong Jae Cho, Han Sung Kim, Seong-Hun Park, Jeunghee Park, Jae-Young Kim, and Bongsoo Kim

J. Phys. Chem. C, **2009**, 113 (17), 7085-7090• DOI: 10.1021/jp900165c • Publication Date (Web): 07 April 2009

Electronic Structure of Vertically Aligned Mn-Doped $CoFe_2O_4$ Nanowires and Their Application as Humidity Sensors and Photodetectors

Chang Hyun Kim, Yoon Myung, Yong Jae Cho, Han Sung Kim, Seong-Hun Park, and Jeunghee Park*

Department of Chemistry, Korea University, Jochiwon 339-700, Korea

Jae-Young Kim

Pohang Accelerator Laboratory, POSTECH, Pohang 790-784, Korea

Bongsoo Kim

Department of Chemistry, KAIST, Daejeon 305-701, Korea

Received: January 7, 2009; Revised Manuscript Received: March 5, 2009

Vertically aligned $CoFe_2O_4$ and 10% Mn-doped $CoFe_2O_4$ nanowires were synthesized by the gas-phase reduction/substitution reaction of pregrown α-Fe_2O_3 nanowires. They consisted of perfect single-crystalline cubic structures grown along the [110] direction. The increase of the lattice constant provides evidence for the effective Mn substitution. We investigated their electronic structures using X-ray absorption spectroscopy and X-ray magnetic circular dichroism. The results suggest that as the Mn substitutes, Mn^{2+}/Mn^{3+} ions would occupy the octahedral (O_h) sites, Mn^{4+} ions form at the tetrahedral (T_d) sites, and a fraction of the Co^{2+} ions migrate from the O_h sites to the T_d sites. The effective Mn substitution can increase the hole concentration, which makes it possible to develop humidity sensors operating at room temperature. Furthermore, it induces high photocurrents upon irradiation of visible light.

1. Introduction

One-dimensional (1D) nanostructures have attracted considerable attention, due to their potential use as building blocks for assembling active and integrated nanosystems.[1] Recently, interest in ferromagnetic iron oxide 1D nanostructures (e.g., nanorods, nanowires, nanobelts, and nanotubes) has been steadily increasing, because of their potential application in perpendicular data recording and spintronic nanodevices.[2,3] Among the many iron oxide materials, cobalt ferrite ($CoFe_2O_4$, Curie temperature (T_C) = 790 K in bulk) has very distinctive properties, such as its huge magnetocrystalline anisotropy, high coercivity, moderate saturation magnetization, unique light-induced coercivity change, high chemical stability, wear resistance, and electrical insulation.[4−8]

$CoFe_2O_4$ has an inverse spinel structure, symbolized as $[Fe^{3+}]_A[Co^{2+}Fe^{3+}]_BO_4$, in which one-eighth of the tetrahedral sites (T_d or A sites) are occupied by Fe^{3+} ions and one-half of the octahedral sites (O_h or B sites) are occupied by Co^{2+} and Fe^{3+} ions.[9] The substitution of other metal ions has been frequently used to modify the magnetic/electrical properties. In particular, extensive studies of Mn-doped $CoFe_2O_4$ have been conducted, which showed that the substitution of Mn for Fe decreases the Curie temperature, magnetic anisotropy, and magnetostriction coefficient.[10−16] A model in which the Mn^{3+} ions enter into the O_h sites and some of the Co^{2+} ions occupy the T_d sites has been used to explain these results, but further clarification is still needed.[12−15] The formation of well-defined single-crystalline $CoFe_2O_4$ nanowire structures would enable us to scrutinize precisely the effect of Mn substitution on their properties. In previous studies, polycrystalline $CoFe_2O_4$ nanowires (NWs) were synthesized inside an anodized aluminum oxide membrane or carbon nanotube templates, using the electrodeposition or sol−gel method.[17−21] Recently, a hydrothermal reaction was developed to synthesize $CoFe_2O_4$ nanobelts.[22] To the best of our knowledge, however, there have been no reports on the synthesis of Mn-doped $CoFe_2O_4$ NWs.

In this study, we synthesized $CoFe_2O_4$ and Mn-doped $CoFe_2O_4$ NW arrays by the gas-phase reduction/substitution reaction of pregrown α-Fe_2O_3 NWs. We investigated how the effective 10% Mn substitution can alter the electronic structures, which ultimately determine the magnetic and electrical properties, using X-ray absorption spectroscopy (XAS) and X-ray magnetic circular dichroism (XMCD). The formation of single-crystalline NWs would enable us to scrutinize precisely the effect of Mn substitution on their electrical properties. As one of their important applications, it is expected that $CoFe_2O_4$ NWs can be used to build gas sensors and photodetectors. We demonstrate that the Mn substituent serves as hole donors to enhance the gas sensing ability and increases the photoconductivity upon visible-light irradiation. Thus, a study of the metal substitution effect is of value from the viewpoint of both fundamental scientific interest and its potential application to various nanodevices.

2. Experimental Section

The $CoFe_2O_4$ and Mn-doped $CoFe_2O_4$ NWs were synthesized by a two-step process: (1) the preparation of α-Fe_2O_3 NWs, and (2) their conversion to $CoFe_2O_4$ and Mn-doped $CoFe_2O_4$ NWs. The vertically aligned α-Fe_2O_3 NWs were prepared by the heating of Fe foil, as described elsewhere.[23] For the conversion reaction, the as-grown α-Fe_2O_3 NWs were placed

* To whom correspondence should be addressed. E-mail: parkjh@korea.ac.kr.

10.1021/jp900165c CCC: $40.75
Published on Web 04/07/2009

inside reactor tubes, and $CoCl_2$ beads (or an $CoCl_2/MnCl_2$ bead mixture) were evaporated at 800 °C using Ar flow for 30 min. The red color of the α-Fe_2O_3 NWs turned black (for both $CoFe_2O_4$ and Mn-doped $CoFe_2O_4$ NWs) after the reaction. The morphology and structures of the products were analyzed by scanning electron microscopy (SEM, Hitachi S-4300), transmission electron microscopy (TEM, Jeol JEM-2010, JEM 2100F), high-voltage TEM (HVEM, Jeol JEM ARM 1300S, 1.25 MV), and energy-dispersive X-ray fluorescence spectroscopy (EDX). High-resolution XRD patterns were obtained using the 8C2 beamline of the Pohang Light Source (PLS) with monochromatic radiation. X-ray photoelectron spectroscopy (XPS) was measured using the 8A1 beamline of the PLS and a laboratory-based spectrometer (ESCALAB 250, VG Scientifics) using a photon energy of 1486.6 eV (Al Kα). The magnetic properties were measured by means of a superconducting quantum interference device (SQUID, Quantum Design) magnetometer.

The XAS and XMCD measurements were carried out at the Pohang Light Source (PLS) elliptically polarized undulator beamline, 2A. The samples were introduced into an experimental chamber with a base pressure of 5×10^{-10} Torr. The spectra were collected in the total electron yield (TEY) mode. A 0.8 T electromagnet was used to switch the magnetization direction. The magnetization direction was flipped between the parallel ($\rho+$) and antiparallel ($\rho-$) directions with respect to the photon helicity vector for each data point. The degree of circular polarization (95%) of the incident light was taken into account in the spectra.

The nanowire array forms a rigid and networked film, so the electrical contacts on the nanowires were made of silver paste. The distance between the electrodes was 1 mm, and the two point probe electrical conductivity measurement was performed using a parametric test equipment (Agilent E5270A). To characterize the visible-region photoresponse, a 450 W Xe lamp was used as the light source with a UV glass filter (Optima Inc.), which transmits light at wavelengths >400 nm.

3. Results and Discussion

3.1. Morphology and Composition. Figure 1a shows a SEM micrograph of the vertically aligned Mn-doped $CoFe_2O_4$ NW array over a large area of the substrates. The magnified image shows that the nanowires have sharp tips and that their roots are attached directly to the substrates (Figure 1b). Their length is 10 μm. The TEM image reveals the bumpy surface of the nanowires (Figure 1c). The inset shows the corresponding selected-area electron diffraction (SAED) pattern, measured at the [111] zone axis, confirming the growth of single-crystalline face-centered cubic (fcc) crystals along the [110] direction. All of the nanowires we observed had the same growth direction. Their average diameter is 250 nm. Figure 1d corresponds to the lattice-resolved image revealing their highly crystalline nature. The distance between the (220) planes (d_{220}) is about 3.0 Å, which is consistent with that of $CoFe_2O_4$ (JCPDS Card No. 22-1086; $a = 8.391$ Å). Figure 1e and 1f displays the EDX mapping and line scanning of Fe, Co, and O elements. The scanning TEM (STEM) images are shown in the left/top image of Figure 1e and in the inset of Figure 1f. The concentration ratio [Fe]/[Co] is estimated to be 2 ± 0.2. The morphology and structure of the $CoFe_2O_4$ NWs are the same as those of the Mn-doped $CoFe_2O_4$ NWs, as shown in the Supporting Information, Figure S1. Figure 1g displays the STEM image and the EDX mapping of Fe, Co, Mn, and O elements. Figure 1h shows the line-scanned profiles of these elements (its STEM image is shown in the inset). The Mn substitution takes place over the entire nanowire with an average content ([Mn]/([Fe] + [Co] + [Mn])) of 0.10 ± 0.03. The EDX data of the $CoFe_2O_4$ and Mn-doped $CoFe_2O_4$ NWs is shown in the Supporting Information, Figure S2. The average value was obtained from the EDX measurement of 3−5 nanowires. Full-range XPS spectra of $CoFe_2O_4$ powder, $CoFe_2O_4$ NWs, and Mn-doped $CoFe_2O_4$ NWs NWs are shown in the Supporting Information, Figure S3. The Mn content is estimated to be about 15% from the integration of the Fe, Co, and Mn peaks, which is close to that of EDX data.

3.2. XRD. We confirmed the complete transformation from α-Fe_2O_3 to $CoFe_2O_4$ phase by the XRD pattern. Figure 2a displays the powder XRD pattern of the Fe_3O_4 powder (Aldrich, 98%), $CoFe_2O_4$ powder (Alfa, 99%), and as-grown $CoFe_2O_4$ and Mn-doped $CoFe_2O_4$ NWs. The peaks can be readily indexed to cubic $CoFe_2O_4$ (JCPDS Card No. 22-1086), showing only a single phase. The peak position of the $CoFe_2O_4$ NWs is matched exactly with that of the $CoFe_2O_4$ powder, but that of the Mn-doped $CoFe_2O_4$ NWs is shifted to a lower angle, i.e., $\Delta(2\theta) = 0.20°$ for the (311) peak and $\Delta(2\theta) = 0.38°$ for the (440) peak, as shown in Figure 2b and 2c. This lower angle shift corresponds to an increase of the lattice constants, suggesting that the larger radius Mn ions effectively substitute for the Fe^{3+} or Co^{2+} ions, as discussed thoroughly in section 3.3. The mismatch with the peak position of Fe_3O_4 powder suggests our correct assignments. Assuming the substitution of Mn^{2+} ions ($r = 97$ pm at O_h) simply for the Co^{2+} ions ($r = 89$ pm at O_h), we estimated the Mn content to be 0.13 by Vegard's law, in which the cell parameter of $Co_{1-x}Mn_xFe_2O_4$ varies linearly with the Mn content for the whole Mn range ($0 \le x \le 1$). This value is surprisingly consistent with the EDX data.

3.3. XAS and XMCD. In order to determine whether Mn substitutes into the T_d or O_h sites, we performed XAS and XMCD measurements. The $CoFe_2O_4$ and 10% Mn-doped $CoFe_2O_4$ NWs are ferromagnetic at room temperature, as shown in section 3.4. The intensity of the spectrum decreases significantly as the temperature decreases, due to the reduced magnetization. Figure 3a shows the Fe $L_{2,3}$ edge ($2p \rightarrow 3d$ transition) XAS and XMCD spectra for the $CoFe_2O_4$ powder, $CoFe_2O_4$ NWs, and Mn-doped $CoFe_2O_4$ NWs, measured at 80 K under $H = 0.8$ T. The spectral feature of the $CoFe_2O_4$ NWs is similar to that of the $CoFe_2O_4$ powders (plotted as reference). These spectra are divided into the L_3 ($2p_{3/2}$) and L_2 ($2p_{1/2}$) regions. The XMCD L_3 region shows the two negative peaks at 708.6 and 710.7 eV corresponding to the Fe^{2+} and Fe^{3+} ions (occupying the O_h sites), respectively, whereas the positive peak at 709.9 eV corresponds to the Fe^{3+} ions at the T_d sites.[24,25] The Mn doping increases significantly the population of Fe^{3+} ions at O_h sites but decreases them at T_d sites. In order to reveal quantitatively the electronic configuration of the Fe atoms at each site, however, atomic multiple calculation should be carried out for both XAS and XMCD spectra, which will be done in the following paper.

Figure 3b shows the Co $L_{2,3}$ edge spectra. The major negative peak at 779.9 eV corresponds to the Co^{2+} ions occupying the O_h sites, which is consistent with previous works on $CoFe_2O_4$ nanopillars embedded in a $BiFeO_3$ film.[26] As the Mn dopes, the positive peak (at 778.8 eV) corresponding to the Co^{2+} ions occupying the T_d sites becomes significant. These may provide evidence for a fraction of the Co^{2+} ions at the O_h sites migrated into the T_d sites by replacing the Fe^{3+} ions, which is consistent with previous work.[11−14] Nevertheless, the quantitative electronic configuration of the Co atom at each site needs further calculation.

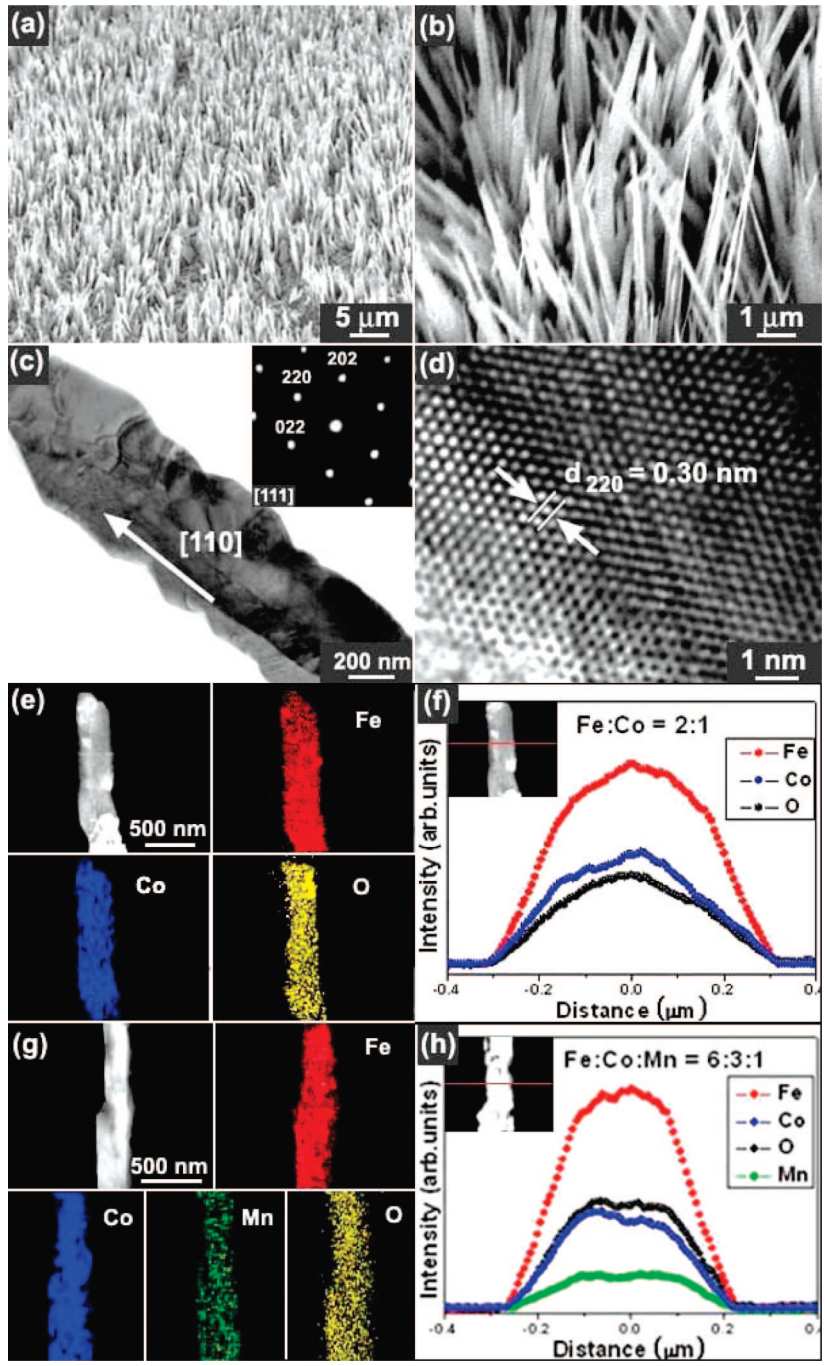

Figure 1. (a) SEM micrographs showing the high-density Mn-doped $CoFe_2O_4$ NW array grown on a large area of the substrates. (b) Magnified view reveals the vertical alignment of the nanowires (length = 10 μm) on the substrates. (c) TEM image shows the uneven surface of the nanowires. The inset shows the corresponding SAED pattern, measured at the [111] zone axis, confirming the [110] growth direction of the single-crystalline $CoFe_2O_4$ NWs. (d) The lattice-resolved image reveals their highly crystalline nature. The distance between the (220) planes (d_{220}) is about 3.0 Å, which is consistent with that of $CoFe_2O_4$ (JCPDS Card No. 22-1086; a = 8.391 Å). (e) EDX mapping and (f) line scanning of Fe, Co, and O elements, showing homogeneous distribution over the whole nanowire. The corresponding STEM image is shown in the left/top image of e and the inset of f. (g) EDX mapping and (h) line scanning of Fe, Co, Mn, and O elements of the Mn-doped $CoFe_2O_4$ NWs, showing the homogeneous Mn distribution, with an average content ([Mn]/([Fe] + [Co] + [Mn])) of 0.10 ± 0.03. The corresponding STEM image is shown in the left/top image of g and the inset of h.

Figure 3c shows the Mn $L_{2,3}$ edge XAS and XMCD spectra for the Mn-doped $CoFe_2O_4$ NWs. The multiplet structure at the Mn L_3 edge is similar in appearance to that of the mixed spinel $La_{1-x}Ca_xMnO_3$ film, which contains Mn^{3+} and Mn^{4+} ions.[27] The negative (at 640.3 and 642.0 eV) and positive peaks (at 644.0 eV) correspond to the Mn^{2+}/Mn^{3+} ions occupying the O_h sites and the Mn^{4+} ions at the T_d sites, respectively. The peak broadening would result from their distorted electronic states. The coexistence of Mn^{4+} and Co^{2+} ions with the Fe^{3+} ions at the T_d sites would maintain the charge balance with the ions at the O_h sites. The presence of the Mn^{4+} ions at the T_d sites was predicted theoretically and suggested as an additional source of magnetorestriction.[10] The present work may provide the first experimental evidence for the presence of Mn^{4+} ions at the T_d sites. Furthermore, a number of research groups have suggested that the Mn^{3+} substitution causes the migration of Co^{2+} to the T_d sites.[12−15] The migration of the Co^{2+} ions is also demonstrated using the XAS and XMCD data. This result provides direct

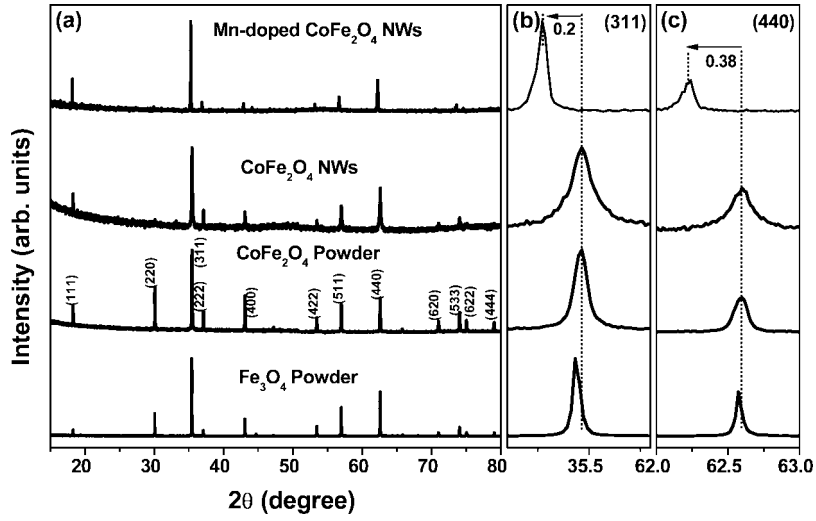

Figure 2. (a) XRD patterns of Mn_3O_4 powder, $CoFe_2O_4$ powder, $CoFe_2O_4$ NWs, and Mn-doped $CoFe_2O_4$ NWs. Magnified scaled (b) (311) and (c) (440) peaks showing the lower angle shift for the Mn-doped $CoFe_2O_4$ NWs.

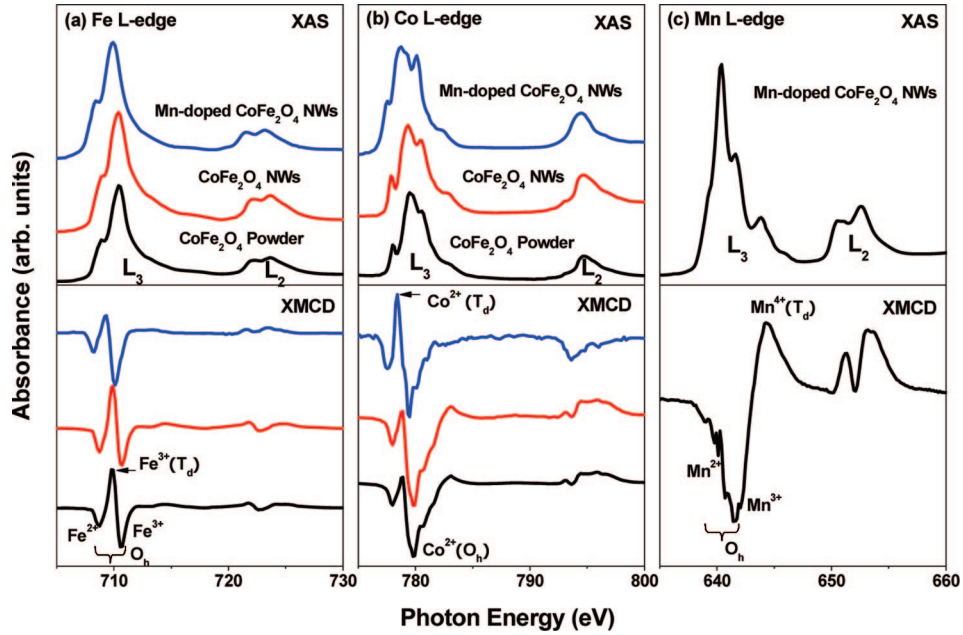

Figure 3. XAS and XMCD spectra of (a) Fe $L_{2,3}$ edge, (b) Co $L_{2,3}$, and (c) Mn $L_{2,3}$ edge of the $CoFe_2O_4$ powder, $CoFe_2O_4$ NWs, and Mn-doped $CoFe_2O_4$ NWs, measured at 80 K under $H = 0.8$ T.

evidence for the origin of the reduced coercivity and resistance of the Mn-doped $CoFe_2O_4$ NWs (as shown in sections 3.4 and 3.5).

3.4. Magnetization. The magnetic properties of two nanowire samples, separated from the substrates, were measured by the SQUID magnetometer. Figure 4 displays the magnetization (M) versus magnetic field (H) curves measured for the $CoFe_2O_4$ and Mn-doped $CoFe_2O_4$ NWs at 300 K. The hysteresis curves of both samples suggest their ferromagnetic behavior. The saturation magnetizations (M_S) of the $CoFe_2O_4$ and Mn-doped $CoFe_2O_4$ NWs are 3 μ_B, and their saturation magnetic fields are 0.5 and 0.1 T, at 300 K, respectively. The hysteresis curve in the vicinity of $H = 0$ reveals that the Mn substitution decreases the coercive field (H_C) from 750 to 70 Oe. The remanence (M_r) of both NWs is about 0.87 μ_B.

The saturated magnetization of the $CoFe_2O_4$ NWs is lower than both the theoretical and experimental value of the $CoFe_2O_4$ single crystals, i.e., 3.65 μ_B.[5] The H_C (750 Oe) at 300 K is lower than that of the film/single crystals (~1700 Oe), comparable to

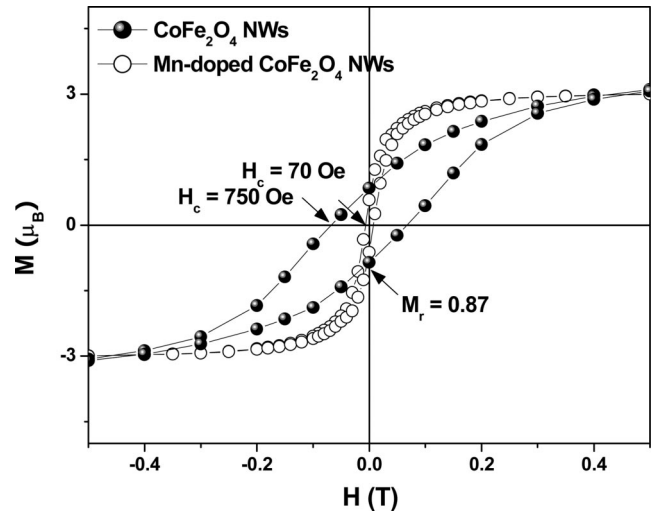

Figure 4. Hysteresis curves of the $CoFe_2O_4$ and Mn-doped $CoFe_2O_4$ NWs measured at 300 K.

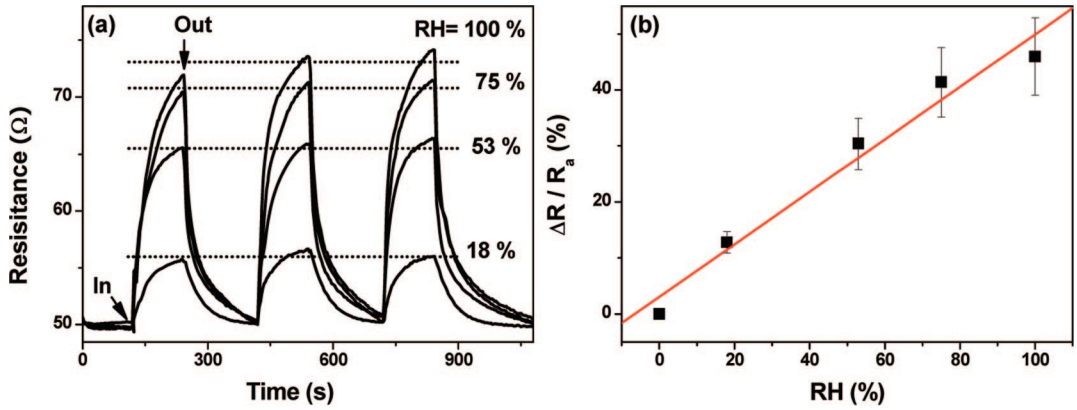

Figure 5. (a) Resistance changes ($\Delta R/R_a$) of the Mn-doped $CoFe_2O_4$ NW array, upon its exposure to water vapor, RH = 18%, 53%, 75%, and 100%. (b) Linear response to the RH.

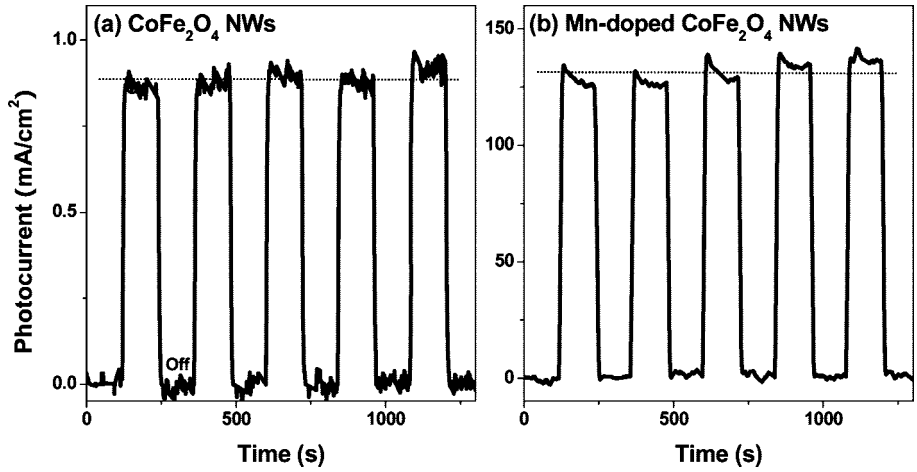

Figure 6. Reversible photoresponse of the (a) $CoFe_2O_4$ and (b) Mn-doped $CoFe_2O_4$ NW array devices as the visible light was turned on and off at different times. The bias voltage was 0.5 V.

that of nanowires (500−1500 Oe), but higher than that of monodispersed nanoparticles (~400 Oe) at 300 K.[6,17b,18−21,28,29] The Mn substitution definitely induces a reduction of the coercivity, which is thought to result from the migration of the Co^{2+} ions from the O_h site to the T_d sites, as already suggested by the XAS and XMCD data.[12−15]

3.5. Application as Gas Sensors and Photodetectors. The nanowire array forms a rigid and networked film, and the aluminum electrodes were deposited on it. The distance between the two electrodes was 1 mm, and the lateral resistance was measured using a two-probe configuration. The measurements of the conductivity of the NW arrays revealed that the Mn substitution increases the conductivity by a factor of ~100 (at room temperature). It is known that the conductivity of spinel ferrites is determined by the electron hopping at the O_h sites.[30,31] The higher conductivity of Mn-doped $CoFe_2O_4$ NWs could be realized by accommodating the conduction path of the ion network at the O_h sites. The migration of Co^{2+} ions into the T_d sites and the substitution of Mn^{2+}/Mn^{3+} ions at the O_h sites (confirmed by the XAS and XMCD measurements) caused an increase in the hole concentration. We suggest that the concentration of holes becomes much larger than that of electrons due to highly oxidized Mn ions, which results in a surface p-type conductivity.

We measured the ability of the air-exposed Mn-doped $CoFe_2O_4$ NWs to be used as a humidity sensor using various relative humidities (RHs) at room temperature. Figure 5a displays the increase in the resistance of the nanowires upon its exposure to the air (1 atm) containing various RHs. The resistance change was plotted for RH = 18%, 53%, 75%, and 100%. Humidity-controlled solutions of saturated LiI, $Mg(NO_3)_2$, NaCl, and pure deionized water in dry air were prepared to provide constant RH values, respectively, at 25 °C. The sensitivity is hereafter defined as $\Delta R/R_a$ ($\Delta R = R_g - R_a$, where R_g and R_a are the resistance under the gas mixture and air, respectively). The change in the resistance reaches a constant value and then recovers during 2 min intervals. A linear response to the RH was observed over the whole RH range, as shown in Figure 5b, suggesting that the nanowire arrays have the potential to be used as humidity sensors.

Gas sensors were also tested using the CoF_2O_4 NWs and showed negligible ability at room temperature, only demonstrating significant sensitivity when the temperature was increased to at least 200 °C. The ethanol gas sensors using the $CoFe_2O_4$ nanocrystals showed sensitivity at a high working temperature (200 °C).[32] Assuming the Mn-doped $CoFe_2O_4$ NWs are p-type semiconductors, as suggested above, the H_2O molecule acts as electron donor: it donates lone pair electrons to the NWs.[33] They react with the surface oxygen ions, freeing electrons that can return to the bands. Electron concentration is increased, and hole concentration is decreased. Downward bending of the bands is small, so the position of the Fermi level is still below the intrinsic level and dominant free charge carriers are still holes: one records the conductance decrease with increasing concentration of H_2O, because the decrease in hole concentration is more important than the increase in electron concentration. The hole doping (i.e., Mn doping) would enhance the sensitivity by making more positive sites (Mn^{2+}/Mn^{3+} ions) available for

withdrawing of electrons from the adsorbed H_2O molecules. The present results certainly provide valuable insights to develop the room-temperature gas sensing model as well as practical sensor devices.

Figure 6 displays the rapid and reversible photoresponse of the $CoFe_2O_4$ and Mn-doped $CoFe_2O_4$ NW array devices (in a vacuum 10^{-3} Torr), as the light source was switched on and off. The photodetector device was biased at 0.5 V. The increase of current density is 0.85 and 130 mA/cm^2, respectively, upon visible light illumination (using UV cutoff filter). The devices can be switched between the low- and the high-conductance states with the response and recovery times estimated to be 6 s. The Mn substitution enhances significantly the photocurrent sensitivity by 150 times. The origin of the higher photocurrent could be attributed to the generation of electron−hole pairs by photons with energy larger than the defect (or impurity) levels that formed significantly by the Mn doping. This fast and high photocurrent sensitivity suggests that these Mn-doped $CoFe_2O_4$ NWs can be suitable candidates as visible light photodetectors or photoswitches.

4. Conclusions

Vertically aligned CoF_2O_4 and 10% Mn-doped CoF_2O_4 NW arrays were synthesized by the gas-phase reduction/substitution reaction of pregrown α-Fe_2O_3 NWs. The average diameter is 250 nm, and the length is 10 μm. They consisted of perfect single-crystalline cubic structures grown along the [110] direction. The XRD patterns confirm their complete conversion to the $CoFe_2O_4$ crystal phase. The Mn substitution decreases the lattice constant, indicating that the Mn ions substitute effectively for the smaller radius Fe or Co ions. The XAS and XMCD data suggest that as the Mn substitutes, the Mn^{2+}/Mn^{3+} ions would enter into the O_h sites, the Mn^{4+} ions occupy the T_d sites, and a fraction of the Co^{2+} ions migrate from the O_h sites to the T_d sites. The magnetization measurements using SQUID reveal that the Mn substitution reduces the coercivity (at 300 K), which can be explained by this electronic structure. The Mn doping would increase the hole concentration, producing p-type semiconductors. We developed highly sensitive humidity sensors using these nanowire arrays, operating at room temperature. The doped Mn ions enhance the sensitivity by making more active sites available for withdrawing of electrons from the H_2O molecules. The Mn doping also allows the NW array to respond more sensitively upon the visible light illumination.

Acknowledgment. This study was supported by KOSEF (R01-2008-000-10825-0; 2008-02364), KRF (2008-314-C00175), and MKE under the ITRC support program supervised by the IITA (2008-C1090-0804-0013). The SEM (Seoul), HVEM (Daejeon), and XRD (Taegu) measurements were performed at the KBSI. The experiments at the PLS were partially supported by MOST and POSTECH.

Supporting Information Available: Additional TEM images, EDX, and XPS data. This material is available free of charge via the Internet at http://pubs.acs.org.

References and Notes

(1) (a) Hu, J.; Odom, T. W.; Lieber, C. M. *Acc. Chem. Res.* **1999**, *32*, 435. (b) Gudiksen, M. S.; Lauhon, L. J.; Wang, J.; Smith, D. C.; Lieber, C. M. *Nature (London)* **2002**, *415*, 617. (c) Duan, X.; Huang, Y.; Agarwal, R.; Lieber, C. M. *Nature (London)* **2003**, *421*, 241.

(2) (a) Han, S.; Li, C.; Liu, Z.; Lei, B.; Zhang, D.; Jin, W.; Liu, X.; Tang, T.; Zhou, C. *Nano Lett.* **2004**, *4*, 1241. (b) Zhang, D.; Liu, Z.; Han, S.; Li, C.; Lei, B.; Stewart, M. P.; Tour, J. M.; Zhou, C. *Nano Lett.* **2004**, *4*, 2151. (c) Liu, Z.; Zhang, D.; Han, S.; Li, C.; Lei, B.; Lu, W.; Fang, J.; Zhou, C. *J. Am. Chem. Soc.* **2005**, *127*, 6.

(3) Liao, Z.-M.; Li, Y.-D.; Xu, J.; Zhang, J.-M.; Xia, K.; Yu, D.-P. *Nano Lett.* **2006**, *6*, 1087.

(4) (a) Goldman, A. *Modern Ferrite Technology*; Van Nostrand Reinhold: New York, 1990. (b) Berkovsky, B. M.; Medvedev, V. F.; Krakov, M. S. *Magnetic Fluids: Engineering Applications*; Oxford University Press: Oxford, 1993. (c) Jakubovics, J. P. *Magnetism and Magnetic Materials*; University Press: Cambridge, 1994.

(5) Slonczewski, J. C. *Phys. Rev.* **1958**, *110*, 1341.

(6) Lee, J. G.; Park, J. Y.; Oh, Y.-J.; Kim, C. S. *J. Appl. Phys.* **1998**, *84*, 2801.

(7) Grigorova, M.; Blythe, J.; Blaskov, V.; Rusanov, V.; Petkov, V.; Masheva, V.; Nihtianova, D.; Martinez, Ll. M.; Munoz, J. S.; Mikhov, M. *J. Magn. Magn. Mater.* **1998**, *183*, 163.

(8) Giri, A. K.; Kirkpatrick, E. M.; Moongkhamklang, P.; Majetich, S. A.; Harris, V. G. *Appl. Phys. Lett.* **2002**, *80*, 2341.

(9) Sawatzky, G. A.; van der Woude, F.; Morrish, A. H. *J. Appl. Phys.* **1968**, *39*, 1204.

(10) Pointon, A. J.; Akers, N. P. *J. Magn. Magn. Mater.* **1982**, *30*, 50.

(11) Abe, M.; Gomi, M. J. *J. Appl. Phys.* **1982**, *53*, 8172.

(12) (a) Zhou, B.; Zhang, Y.-W.; Liao, C.-S.; Cheng, F.-X.; Yan, C.-H.; Chen, L.-Y.; Wang, S.-Y. *Appl. Phys. Lett.* **2001**, *79*, 1849. (b) Zhou, B.; Zhang, Y.-W.; Liao, C.-S.; Yan, C.-H. *J. Magn. Magn. Mater.* **2002**, *247*, 70.

(13) (a) Krieble, K.; Schaeffer, T.; Paulsen, J. A.; Ring, A. P.; Lo, C. C. H.; Snyder, J. E. *J. Appl. Phys.* **2005**, *97*, 10F101. (b) Paulsen, J. A.; Ring, A. P.; Lo, C. C. H.; Snyder, J. E.; Jiles, D. C. *J. Appl. Phys.* **2005**, *97*, 044502. (c) Melikhov, Y.; Snyder, J. E.; Jiles, D. C.; Ring, A. P.; Paulsen, J. A.; Lo, C. C. H.; Dennis, K. W. *J. Appl. Phys.* **2006**, *99*, 08R102.

(14) (a) Bhame, S. D.; Joy, P. A. *J. Appl. Phys.* **2006**, *99*, 073901. (b) Bhame, S. D.; Joy, P. A. *J. Appl. Phys.* **2006**, *100*, 113911.

(15) Kim, K. J.; Kim, H. K.; Park, Y. R.; Park, J. Y. *J. Magn. Magn. Mater.* **2006**, *304*, e106.

(16) Caltun, O.; Rao, G. S. N.; Rao, K. H.; Rao, B. P; Dumitru, I.; Kim, C.-O.; Kim, C.-G. *J. Magn. Magn. Mater.* **2007**, *316*, e618.

(17) (a) Pham-Huu, C.; Keller, N.; Estournès, C.; Ehret, G.; Ledoux, M. J. *Chem. Commun.* **2002**, 1882. (b) Pham-Huu, C.; Keller, N.; Estournès, C.; Ehret, G.; Grenèche, J. M.; Ledoux, M. J. *Phys. Chem. Chem. Phys.* **2003**, *5*, 3716. (c) Keller, N.; Pham-Huu, C.; Estournès, C.; Grenèche, J. M.; Ehret, G.; Ledoux, M. J. *Carbon* **2004**, *42*, 1395. (d) Tessonnier, J. P.; Winé, G.; Estournès, C.; Leuvrey, C.; Ledoux, M. J.; Pham-Huu, C. *Catal. Today* **2005**, *102*, 29.

(18) Ji, G.; Tang, S.; Xu, B.; Gu, B.; Du, Y. *Chem. Phys. Lett.* **2003**, *379*, 484.

(19) Jung, J.-S.; Lim, J.-H.; Choi, K.-H.; Oh, S.-L.; Kim, Y.-R.; Lee, S.-H.; Smith, D. A.; Stokes, K. L.; Malkinski, L.; O'Connor, C. J. *J. Appl. Phys.* **2005**, *97*, 10F306.

(20) Carlier, D.; Ansermet, J.-P. *J. Electrochem. Soc.* **2006**, *153*, C277.

(21) Hua, Z. H.; Chen, R. S.; Li, C. L.; Yang, S. G.; Lu, M.; Gu, B. X.; Du, Y. W. *J. Alloys Compd.* **2007**, *427*, 199.

(22) Liu, H.; Hu, C.; Wang, Z. L. *Nano Lett.* **2006**, *6*, 1535.

(23) Kim, C. H.; Chun, H. J.; Kim, D. S.; Kim, S. Y.; Park, J.; Moon, J. Y.; Lee, G.; Yoon, J.; Jo, Y.; Jung, M.-H.; Jung, S. I.; Lee, C. J. *Appl. Phys. Lett.* **2006**, *89*, 223103.

(24) van der Lann, G.; Thole, B. T. *Phys. Rev. B* **1991**, *43*, 13401.

(25) Pattrick, R. A. D.; Van Der Laan, G.; Henderson, C. M. B.; Kuiper, P.; Dudzik, E.; Vaughan, D. J. *Eur. J. Mineral.* **2002**, *14*, 1095–1102.

(26) Zhao, T.; Scholl, A.; Zavaliche, F.; Zheng, H.; Barry, M.; Doran, A.; Lee, K.; Cruz, M. P.; Ramesh, R. *Appl. Phys. Lett.* **2007**, *90*, 123104.

(27) Song, J. H.; Park, J.-H.; Kim, J.-Y.; Park, B.-G.; Jeong, Y. H.; Noh, H.-J.; Oh, S.-J.; Lin, H.-J.; Chen, C. T. *Phys. Rev. B* **2005**, *72*, 060405(R).

(28) Sun, S.; Zeng, H.; Robinson, D. B.; Raoux, S.; Rice, P. M.; Wang, S. X.; Li, G. *J. Am. Chem. Soc.* **2004**, *126*, 273.

(29) Wang, W. H.; Ren, X. *J. Cryst. Growth* **2006**, *289*, 605.

(30) Cullen, J. R.; Callen, E. *J. Appl. Phys.* **1970**, *41*, 879.

(31) Zhang, Z.; Satpathy, S. *Phys. Rev. B* **1991**, *44*, 13319.

(32) Xiangfeng, C.; Dongli, J.; Yu, G.; Chenmou, Z. *Sens. Actuators B* **2006**, *120*, 177.

(33) (a) Gurlo, A.; Riedel, R. *Angew. Chem., Int. Ed.* **2007**, *46*, 3826. (b) Gurlo, A.; Bârsan, N.; Oprea, A.; Sahm, M.; Weimar, U. *Appl. Phys. Lett.* **2004**, *85*, 2280.

JP900165C